Nanocrystalline cerium-doped Y-type barium hexaferrite; a useful catalyst for selective oxidation of styrene

Mukesh Suthar[1] · Avinash K. Srivastava[2] · Raj K. Joshi[2] · P. K. Roy[1]

Abstract

The cerium-doped Y-type barium hexaferrites $Ba_{2-x}Ce_xCo_2Fe_{12}O_{22}$ ($x = 0.0, 0.1, 0.2$, and 0.3) were synthesized using the sol–gel auto combustion method. The synthesized nanocrystalline hexaferrite powders were characterized; especially it's structural, morphological, and magnetic properties, through X-ray diffractometer, FTIR spectroscopy, scanning electron microscopy and vibrating sample magnetometer, respectively. The effects of catalyst amount, reaction temperature and time, solvent and oxidizing agent required for the entire conversion of styrene to benzaldehyde were also examined with pure Y-type barium hexaferrite (BrM). The catalytic performance of the BrM powder was measured for its suitability in the oxidation of styrene using various oxidants, and the isolated yield of the benzaldehyde was calculated using the column chromatography separation. The as-prepared 20 mg BrM samples showed total conversion of styrene and 66% isolated yield for benzaldehyde at 120 °C for 24 h in the presence of trifluoroacetic acid as an oxidant. The effect of cerium doping on the benzaldehyde selectivity was also analyzed at optimized conditions and found that cerium-doped samples showed excellent catalytic performance. Paralleled with the pristine barium hexaferrite, the catalytic efficiency was significantly enriched and exhibited its maximum performance with $Ba_{1.8}Ce_{0.2}Co_2Fe_{12}O_{22}$ ferrite, almost 71% selectivity was achieved with the same reaction conditions. This enhanced performance was correlated with the XPS studies for $x = 0.2$ sample. The as-prepared catalyst was magnetically separable to reprocess. There was no remarkable loss of catalytic activity when it was reprocessed for five consecutive trials.

1 Introduction

Recently, hexagonal ferrites are well recognized magnetic materials in various application fields. These ferrites can be used as economical hard magnets along with making of components for high-frequency applications. Attentiveness in Y-type nano hexaferrite has been reawakened due to their multiferroic properties. Y-type barium hexaferrite widely uses as permanent magnets, high-density magneto-optical, contact-based recording media, overcoat free, and applicable high-frequency devices because to their greater chemical stability, excellent mechanical hardness, wear and corrosion resistance, and higher value of Curie temperature [1]. These ferrites can also be used as a catalyst because of magnetic recycling and redox characteristics [2]. Nanometer-sized ferrite catalyst may enhance its catalytic activity. The catalytic efficiency of any ferrite system is due to the capability of metallic ions to wander among the sub-lattices without destroying the initial structure. Moreover, there is a need to come up with catalysts that can be reusable, better selective, better active, and more facile to separate.

In general, ferrites are mostly employed as catalysts in liquid phase reactions synthesis, e.g., decomposition of hydrogen peroxide (H_2O_2) [2], oxidative dehydrogenation of hydrocarbons [3, 4], handling and treatment of exhaust gases [5], oxidation of chloro-benzene and phenol hydroxylation [6], hydrous desulphurization of petroleum products [6], and combustion reaction of methane [7, 8]. Conventionally, these liquid phase reactions can be performed with both heterogeneous and homogeneous catalyst systems [9, 10]. Recently, homogeneous catalysts become less

✉ P. K. Roy
  pkroy.cer@itbhu.ac.in

[1] Department of Ceramic Engineering, IIT (BHU), Varanasi, UP 221005, India

[2] Department of Chemistry, Malaviya National Institute of Technology Jaipur, Jaipur, Rajasthan 302017, India

attractive than heterogeneous catalysts due to inconvenient separating processes for products and catalysts [11]. Various ferrite catalysts, such as nickel and zinc ferrites, Fe_3O_4 [8], $Ce_xCo_{1-x}Fe_2O_4$ [12], $SrFe_2O_4$ [13], $Mg_xFe_{3-x}O_4$ [14], $CaFe_2O_4$ [15], $NiFe_{2-x}Gd_xO_4$ [16], $Mg_{1-x}Cu_xFe_2O_4$ [17], $CoFe_2O_4$ [18], Fe_2O_3 [19], and $MnFe_2O_4$ [20] have been investigated to catalyze styrene oxidation reaction in presence of hydrogen peroxide (H_2O_2), O_2 and tert-butyl-hydroperoxide (t-BuOOH) as an oxidant.

The major issue of the selective oxidation of styrene is due to intricate preparation techniques, high costs of catalysts or oxidants, severe conditions, and low conversion efficiency. Nowadays, it is a crucial importance to achieve a suitable catalyst, which can support the oxidation reaction of styrene at side chains for both theoretical research and applicable for the industrially adoptable process [21]. The products of this reaction include benzaldehyde (C_6H_5CHO), which is a priceless chemical that has extensive applications in organic synthesis related to pharmaceuticals, perfumery, agrochemical industries, dyestuffs, and production of various other aldehydes [22, 23].

We have attempted to use cerium-doped Y-type nano hexaferrite as catalysts for the oxidation of styrene. The circumstances for achieving the maximum conversion of styrene in addition to higher selectivity of desired product, different experimental parameters, such as various oxidizing agents, reaction time, amount of catalyst, and temperature, have been exploited. The synthesized cerium-doped Y-type hexaferrite nanoparticles are successfully used as magnetically recoverable and heterogeneous catalysts for styrene oxidation in the presence of trifluoroacetic acid (TFA) as oxidant. It is observed that the presence of TFA accelerates the oxidation [24] and also contributes to lowering the risk of handling (explosiveness) during the process at ambient temperature [25] as compared with a widely used oxidant like hydrogen peroxide (H_2O_2). Here, we have reported cerium-doped Y-type hexaferrite, synthesized via sol–gel auto combustion method, which can capably catalyze the oxidation of styrene to turn out benzaldehyde in water/methanol mixture as solvent using TFA as oxidant. The advantage of the sol–gel auto combustion process is to promote thermally induced redox anionic reaction. It can be considered as one of the efficient methods to produce ferrites at the nanoscale with excellent phase homogeneity.

2 Experimental

Ultrafine nanoparticles of $Ba_{2-x}Ce_xCo_2Fe_{12}O_{22}$ ($x = 0.0$, 0.1, 0.2, and 0.3) ferrites were prepared by the auto combustion route using metal nitrate as precursors. The stoichiometric amounts of barium nitrate [$Ba(NO_3)_2$], cerium nitrate [$Ce(NO_3)_3·6H_2O$] cobalt nitrate [$Co(NO_3)_3·6H_2O$], ferrous nitrate [$Fe(NO_3)_3·9H_2O$], and citric acid [$C_6H_8O_7·H_2O$] were dissolved in the least amount of deionized (DI) water to make the solution of 1:1 (metal nitrates: citric acid) molar ratio. The pH of the solution was tuned at 7 by adding liquid ammonia to the solution. The solution was kept maintained at 80 °C temperature to transform a gel, which further was ignited and burnt in ashes by the auto combustion process. The burnt ash powders were ground and calcined in an oxidizing atmosphere at 1200 °C for 2 h at a heating rate of 3 °C per minute. Finally, the sample was crushed and sorted by a 250 mesh sieve prior to further catalysts characterizations.

The phase identification was made by X-ray diffraction (XRD) measurement in the range 20°–80° with a step size of 0.02° using Rigaku Miniflex 600 benchtop with Cu–kα radiation. FTIR spectra of the calcined powders were examined in transmittance mode in the range of 4000–400 cm^{-1} using Perkin Elmer BXIII FTIR infrared spectrometer. The surface area of the calcined ferrite was determined using Quanta-chrome Autosorb (Model No: Nova 1200 BET). The surface morphology of the powder was observed by SEM (ZEISS, EVO 18-2045) and the elemental mapping by EDX. The magnetic measurements of the powders were carried out at room temperature using SQUID MPMS (Quantum design, Model-MPMS 3, EM-QM, USA) with a maximum magnetic field of 7×10^4 Oe. The chemical states of surface elements were analyzed using an X-ray photoelectron spectrometer (XPS) (ESCALAB-250 (1×10^{-9} bar) with AlKα X-ray source and a mono chromator, Thermo Fisher Scientific Inc., Waltham, UK). The reaction products were examined by column chromatography and confirmed with ^1H, $^{13}C\{^1H\}$ NMR spectra, recorded using JEOL ECS-400 spectrometer (operating at 400 MHz for ^1H and 100 MHz for ^{13}C).

The selective oxidation of styrene was evaluated with styrene (1 Equiv), TFA (1 Equiv), and 20 mg of pure barium hexaferrite powder as a catalyst for a typical procedure. All the ingredients were mixed in a reaction tube along with 1.5 ml of aqueous methanol: water (3:2) solution as a solvent. The resulting reaction mixture was continuously stirred in a sealed reaction tube as per the desired period and desired temperature using an oil bath. After completion of the reaction, the mixture was cooled down at room temperature, and the product was extracted through solvent extraction using ethyl acetate (20 ml) twice. The extracted product was further washed with the water and dried over anhydrous Na_2SO_4. The solvent was evaporated at reduced pressure on a rotary evaporator. The formation of the desired product was confirmed through thin layer chromatography (TLC) co-spotting method with the standards as a reference. An incurred crude product was purified by silica-gel column chromatography using ethyl acetate/hexane dilute the mixture. Finally, obtained solid/liquid product was then characterized by ^1H and ^{13}C NMR spectroscopy analysis.

3 Results and discussion

3.1 Characterization of the ferrite (catalysts)

3.1.1 Phase analysis

The XRD pattern of the calcined cerium-doped barium hexaferrite is shown in Fig. 1a. It is confirmed that the single Y-type barium hexaferrite phase is formed after calcination at 1200 °C. Cerium-doped samples show cerium oxide as an impurity phase. The peaks obtained in the XRD pattern for these hexaferrite samples match exactly with the standard JCPDS card no 440206 for $Ba_2Co_2Fe_{12}O_{22}$ and JCPDS card no 750390 for CeO_2 as an impurity phase. The average crystallite size, lattice parameters along with c/a ratio, cell volume, surface area, and X-ray density are shown in Table 1. Structural parameters such as crystallite size, lattice constants (a and c), unit cell volume, X-ray density, and are calculated using the following Eqs. 1, 3, 4 and 5, respectively [26]

$$\text{Crystallite size} = \frac{k\lambda}{B\cos\theta} \qquad (1)$$

where λ (1.54056 Å) is the X-ray wavelength, θ is the Bragg's angle, B is the full width at half maximum, and k is

the Sherrer's constant. Line broadening due to instrument is subtracted from the peak width before calculating the crystallite size using the following Eq. (2):

$$B^2 = B_{\text{meas}}^2 - B_{\text{equip}}^2 \qquad (2)$$

where, B_{meas} = measured full width at half maximum from the peak, B_{equip} = instrumental broadening.

$$\frac{1}{d_{hkl}^2} = \frac{4}{3}\left(\frac{h^2 + hk + k^2}{a^2}\right) + \frac{l^2}{c^2} \qquad (3)$$

where, d_{hkl} is the d-spacing value of the corresponding Miller indices (h, k, and l).

$$V = a^2 c \sin 120° \qquad (4)$$

$$d_x = \frac{Z \cdot M}{Na \cdot V} \qquad (5)$$

where Z is the effective number of molecules per unit cell, in case of Y-type hexaferrite its value is 3 due to the overlapping of T and S blocks [3(TS)] and oxygen layers, M is the molecular mass of the sample, N_a is Avogadro's number, and V is referred for unit cell volume of a specific sample. The X-ray pattern reveals that the Ce^{3+} can be nearly substituted in the composition of $Ba_{2-x}Ce_xCo_2Fe_{12}O_{22}$ ferrite. The

Fig. 1 **a** XRD patterns of calcined $Ba_{2-x}Ce_xCo_2Fe_{12}O_{22}$ ($x=0.0$, 0.1, 0.2, and 0.3) ferrites, **b** Peak shifting of (110) and (1013) peaks
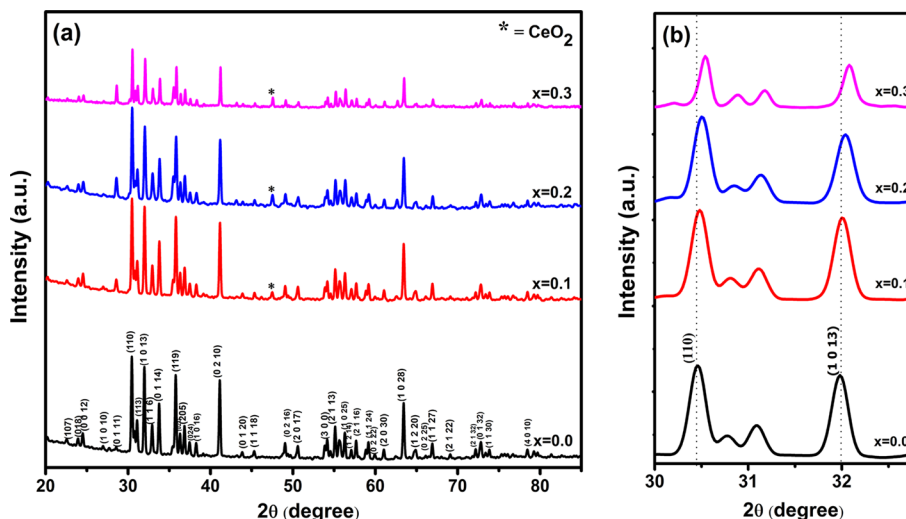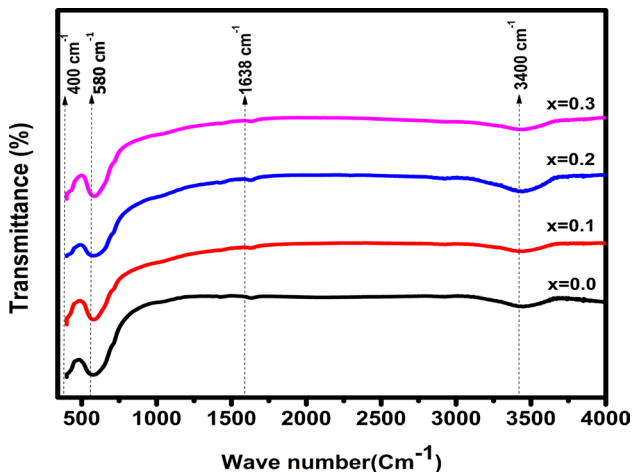
Table 1 Crystallite size, lattice parameters, c/a ratio, cell volume, surface area, and X-ray density of $Ba_{2-x}Ce_xCo_2Fe_{12}O_{22}$ ($x=0.0$, 0.1, 0.2, and 0.3) ferrites

Sample	Crystallite size (nm)	a (Å)	c (Å)	c/a	Cell volume (Å³)	Surface area (m²g⁻¹)	X-ray density (g/cm³)
$Ba_2Co_2Fe_{12}O_{22}$	48.02	5.866	43.562	7.426	1298.194	39	5.428
$Ba_{1.9}Ce_{0.1}Co_2Fe_{12}O_{22}$	47.41	5.866	43.545	7.423	1297.598	43	5.432
$Ba_{1.8}Ce_{0.2}Co_2Fe_{12}O_{22}$	44.58	5.866	43.492	7.414	1296.019	47	5.439
$Ba_{1.7}Ce_{0.3}Co_2Fe_{12}O_{22}$	45.40	5.866	43.476	7.411	1295.580	44	5.443

peak intensity corresponding to the CeO_2 impurity phase gets stronger with the substitutional amount [27, 28]. This suggests that the limit of solubility of doped cerium in ferrite is achieved in the composition. A similar, dual-phase system in barium hexaferrite with Ce substitution is also observed by Vakil et al. [29]. A minor reduction in the lattice constant and right-hand side shifting (Fig. 1b) of Bragg peak position corresponding to (110) and (1013) can be detected. It depicts the replacement of larger ion Ba^{2+} (1.34 Å) with a smaller doped ion Ce^{3+} (1.034 Å). The crystallite size, as well as the cell volume, also decreases with Ce^{3+} substitution in the ferrites. It can also be found that the addition of cerium also leads to an increase in the surface area. An increase in X-ray density is attributed due to the higher atomic mass of Ce^{3+} in comparison with Ba^{2+}.

3.1.2 FTIR analysis

FTIR is employed to evaluate the chemical bonding present in the as-synthesized samples calcined at 1200 °C, as shown in Fig. 2. Bands between 400 and 800 cm^{-1} are the major characteristic bands of the ferrite [30]. A slight shifting of these characteristic bands towards the higher wavenumber with substitution is due to the decreasing of cell volume [31]. Two absorption peaks around 580 cm^{-1} and 400 cm^{-1}

Fig. 2 FTIR spectra of calcined $Ba_{2-x}Ce_xCo_2Fe_{12}O_{22}$ ($x = 0.0$, 0.1, 0.2, and 0.3) ferrite powders

are observed in all these samples corresponding to the tetrahedral and octahedral metal ion vibrations, respectively. It is assigned due to the expansion of metal–oxygen bonds. It may be due to Fe–O stretching and attributed to the formation of hexaferrite [32]. The vibrational frequency for Fe–O bond can be resolute by the following Eq. (6) [33]

$$v = \frac{\sqrt{t/\mu}}{2\pi l} \tag{6}$$

where v is wave number corresponding to the absorption peak, l is the velocity of light, t is the average force constant in case of Fe–O bond and μ is the effective mass of the Fe–O bond calculated using the Eq. (7):

$$\mu = \frac{M_O \times M_{Fe}}{M_O + M_{Fe}} \tag{7}$$

where, M_O and M_{Fe} are the atomic weight of oxygen and iron, respectively. The force constant (t) can be interrelated with the typical Fe–O bond length (r) by the Eq. (8):

$$t = 17/r^3 \tag{8}$$

By using the above equations, the values of force constant and bond lengths for Fe–O are calculated from the FTIR spectra data and are tabulated in Table 2. It is confirmed that the addition of cerium leads to decreasing bond lengths, also confirms the contraction of cell volume, as obtained in the X-ray diffraction pattern. Apart from these characteristic bands, another absorption peak around 1638 cm^{-1} is also found. It can be correlated to the presence of the N–H band that can be due to the use of ammonia solution to adjust the pH. It is also found a broader absorption peak around 3400 cm^{-1} for O–H stretching, which can be attributed to the presence of some moisture in the samples [34, 35].

3.1.3 Microstructure analysis

The microstructure of the calcined pure Y-type barium hexaferrite powder is shown in Fig. 3 along with EDX and elemental mapping micrograph. SEM micrograph of the calcined powder reveals that these particles are homogeneous with a nearly hexagonal plate-like shape in a range of
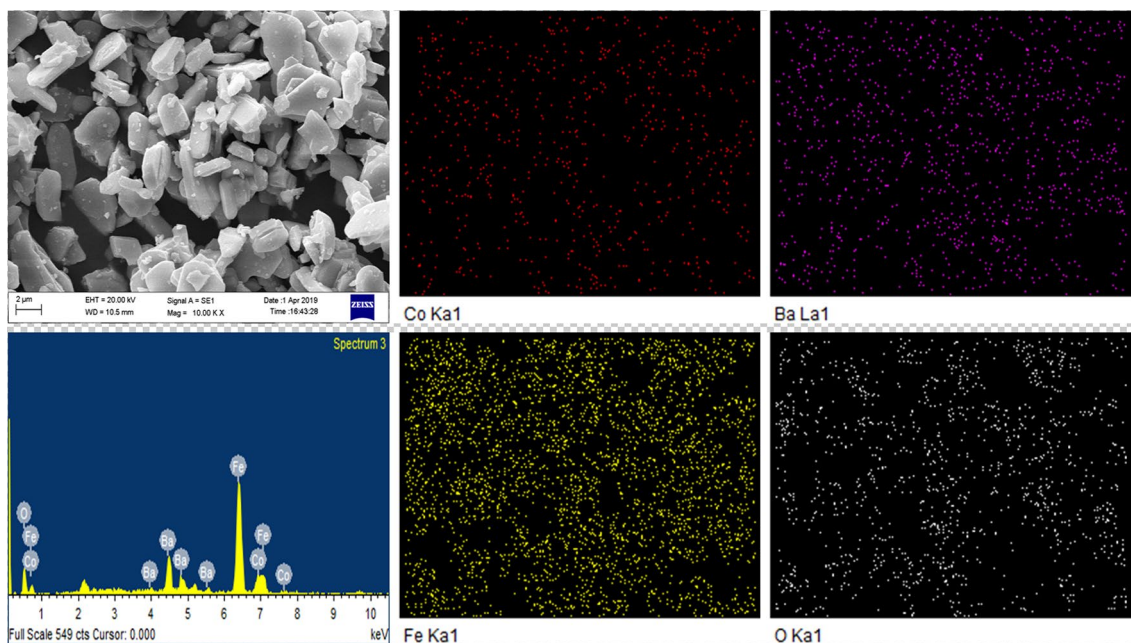
Table 2 Wave number, effective mass, force constant, and bond length of $Ba_{2-x}Ce_xCo_2Fe_{12}O_{22}$ ($x = 0.0$, 0.1, 0.2, and 0.3) ferrites

Sample	Wave number (cm^{-1})	Effective mass (10^{-26} kg)	Force constant k (N/cm)	Bond length (Fe–O) (Å)
$Ba_2Co_2Fe_{12}O_{22}$	577.57	2.065	2.446	1.908
$Ba_{1.9}Ce_{0.1}Co_2Fe_{12}O_{22}$	580.46	2.065	2.471	1.902
$Ba_{1.8}Ce_{0.2}Co_2Fe_{12}O_{22}$	581.43	2.065	2.479	1.899
$Ba_{1.7}Ce_{0.3}Co_2Fe_{12}O_{22}$	584.80	2.065	2.508	1.892

Fig. 3 SEM, EDX, and Elemental mapping micrographs of calcined pure Y-type barium hexaferrite powder

0.5–2.8 μm with an average size of 1.96 μm. To conclude the chemical composition and homogeneity of the sample, the EDX is performed, and the outcome of the EDX analysis appraises the atomic weight percentage of constituting cations in the investigated samples. It is found that the % of cations is nearly accurate, corresponding to the composition ratio of (1:1:6:11) in the desired formula. The elemental mapping micrographs of the ferrite shows that Co, Ba, Fe, and O are distributed uniformly in the sample and confirm the purity of the sample.

3.1.4 Magnetic analysis

The small amount of Ce^{3+} ions doping at the place of Ba^{2+} shows a significant impact on the magnetic properties in $Ba_2Co_2Fe_{12}O_{22}$ ferrite. Figure 4 shows the magnetic hysteresis loops of $Ba_{2-x}Ce_xCo_2Fe_{12}O_{22}$ ferrite powders measured at 300 K under the maximum applied field of 70 kOe. The hysteresis loop (M–H curve) of all these powder samples shows ferrimagnetic behavior, and the magnetic parameters are tabulated in Table 3. The Bohr magnetron number can be estimated by using saturation magnetization (M_s) and molecular weight (W) with the following Eq. (9) [26]:

$$n_B = \frac{W \times M_s}{5585} \tag{9}$$

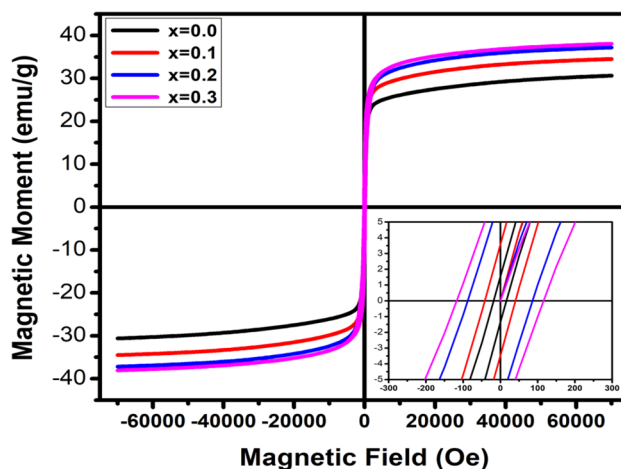As the cerium content increased, the value of Bohr magneton (n_B) and saturation magnetization (M_s) increases

Fig. 4 M versus H plot of calcined $Ba_{2-x}Ce_xCo_2Fe_{12}O_{22}$ (x = 0.0, 0.1, 0.2, and 0.3) ferrite powders at room temperature

Table 3 Magnetic parameters n_B, M_s, M_r, M_r/M_s, H_c of $Ba_{2-x}Ce_xCo_2Fe_{12}O_{22}$ (x = 0.0, 0.1, 0.2, and 0.3) ferrites

Sample	n_B (μB)	M_s (emu/g)	M_r (emu/g)	M_r/M_s	H_c (Oe)
$Ba_2Co_2Fe_{12}O_{22}$	7.74	30.58	1.55	0.051	16.97
$Ba_{1.9}Ce_{0.1}Co_2Fe_{12}O_{22}$	8.73	34.46	3.62	0.105	41.15
$Ba_{1.8}Ce_{0.2}Co_2Fe_{12}O_{22}$	9.42	37.16	6.62	0.178	86.92
$Ba_{1.7}Ce_{0.3}Co_2Fe_{12}O_{22}$	9.63	38.03	7.82	0.206	116.75

continuously and reaches up to the value of 9.63 μB and 38.03 emu/g at $x = 0.3$. It can be interpreted based on the replacement of a magnetic ion Ce^{3+} (having 1 μB magnetic moment) with a nonmagnetic Ba^{2+} ion [27, 28, 35]. The coercivity (H_c) also follows the same increasing trend with Ce^{3+}, and it is found to be the maximum value of 116.75 Oe, at $x = 0.3$. It may be explained by the existence of low spin Fe^{2+} ions along with high spin Fe^{3+}, and it increases with cerium addition, results in greater coercive force [36]. The squareness ratio ($S = M_r/M_s$) is also an important characteristic parameter to determine the order of the magnetic hardness of any material. It shows a similar magnetic profile with soft ferrite (especially nickel ferrite nanoparticles $M_s = 36.72$ emu/g, $H_c = 49.65$ Oe), cerium-doped Y-type barium hexaferrite $Ba_{2-x}Ce_xCo_2Fe_{12}O_{22}$ may also be investigated in the oxidation of styrene [8, 37].

3.2 Catalytic activity studies

The reaction, which involves the oxidation of hydrocarbon to oxygenic compounds, is an essential part of the research in organic chemistry. Generally, the soft ferrites are identified as efficient oxidation catalysts and applied to transfer an oxygen atom from the oxidizing agent into hydrocarbon molecules present in the organic solvent [38]. Here, $Ba_2Co_2Fe_{12}O_{22}$, synthesized by sol–gel auto combustion method, is used as a catalyst to evaluate its catalytic efficiency. The oxidation reaction of styrene is used as a model reaction to evaluate its catalytic activity and results to form benzaldehyde and other minor products [39]. It is the first attempt to use a hard magnetic ferrite as a catalyst in the oxidation of styrene as per Scheme 1.

To confirm the need of the hexaferrite for selective oxidation of styrene, a blank reaction is conducted under similar conditions. As a result, there is no reaction taken place under the absence of the catalyst. To achieve the optimized conditions for this reaction, styrene is studied as a model substrate using TFA (trifluoroacetic acid) as an oxidant in the presence of various catalytic amounts of pure undoped Y-type barium hexaferrite. According to Vishnetskaya et al. TFA is found to be a promising oxidizing agent to activate the molecular oxygen dissolved in it, and it endows the acid with robust oxidizer properties [40]. The amount of catalyst, reaction time, reaction temperature, and solvent are optimized for this model reaction. Due to the economic and environmental

advantages, the mixture of water with methanol is selected as a solvent instead of other organic solvents like acetonitrile [41], acetone [39], chloroform [42], 1,2-dichloroethane [42], 1,2-dichloromethane [41], ethyl acetate [41], etc.

3.2.1 Influence of catalyst amount

Figure 5 displays the influence of catalyst amount on the conversion and the selectivity of styrene after oxidation. It can be seen that initially, the conversion with lower addition (up to 5 mg) of barium hexaferrite is too less. Further increasing the amount of catalyst, the selectivity of benzaldehyde is increased. The increment in the catalyst amount from 10 to 15 mg results to 88% improvement, and from 15 to 20 mg results in 40.42% improvement of yield for benzaldehyde selectivity in the final product. This may be due to the accessibility of quite large surface area and more number of active sites, which help the scattering of species. With further increase up to 25 mg, it doesn't show further enhancement in the selectivity. It may be due to magnetic agglomeration that results in a lower contact area for reactants [12]. It may also due to the adsorption of reactants on different catalyst particles, thus decreasing the chance to interrelate. The best selectivity of benzaldehyde is found at
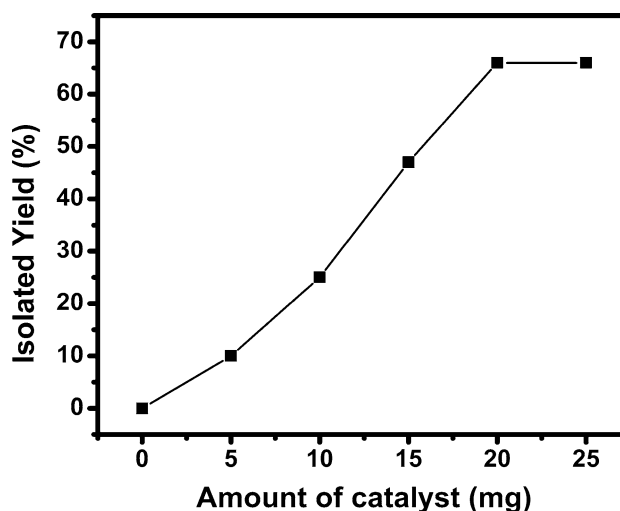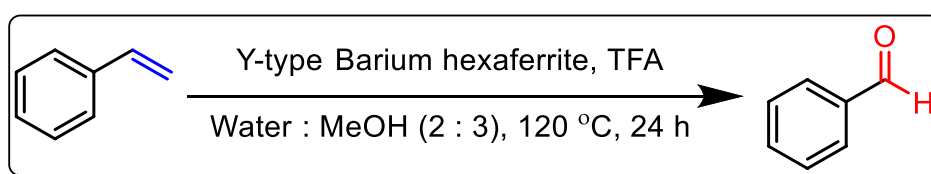

Fig. 5 Influence of catalyst amount on the isolated yield for styrene in reaction product (Reaction conditions; Temperature 120 °C, Time 24 h with TFA)

Scheme 1 Transformation of styrene to benzaldehyde in the catalytic presence of Y-type barium hexaferrite and TFA

Y-type Barium hexaferrite, TFA

Water : MeOH (2 : 3), 120 °C, 24 h

20 mg of the catalyst with TFA as an oxidizing agent, and 20 mg is selected as the optimum catalyst amount for further processing.

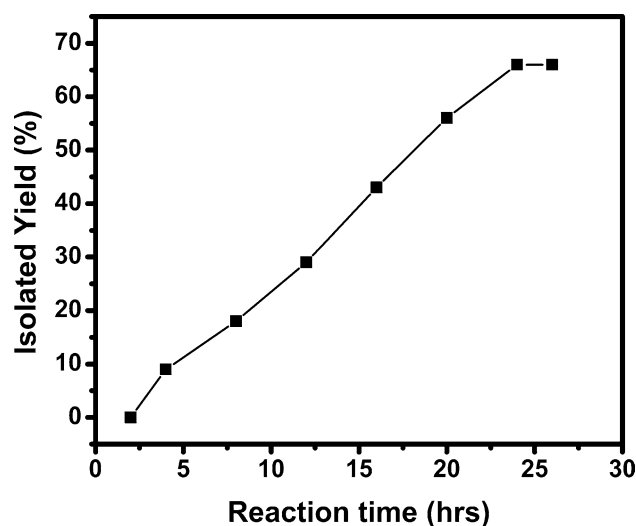### 3.2.2 Influence of reaction temperature

The impacts of reaction temperature on the styrene oxidation are estimated in the temperature range between 60 to 140 °C with the optimum catalyst amount (20 mg) and TFA as an oxidizing agent for 24 h reaction. The result is shown in Fig. 6. It can be found that high temperature prefers in both conversion and selectivity of benzaldehyde in the reaction product. It is revealed that the selectivity of benzaldehyde increases continuously with each step of 10 °C from 60 to 120 °C, respectively, and remain constant after that. This suggests that with increasing temperatures, the bond C=C cleavage is more constructive. Above 120˚C, the increasing rate of selectivity becomes constant due to the faster evaporation rate of the solvent. Considering the energy balance, the best selectivity of benzaldehyde is found to be 66% at 120 °C with 20 mg of catalyst.

3.2.3 Influence of reaction time

The effect of reaction time on the oxidation of styrene is inspected in the range of 2 to 26 h with the optimum amount of catalyst (20 mg) along with TFA as an oxidizing agent at 120 °C. Figure 7 shows that the selectivity of the benzaldehyde is increased with the reaction time up to 24 h. After 24 h, the selectivity of the desired product becomes stable at 66% due to the enhanced reaction time, which allows the formation of the byproducts. It may impede the further yield of the desired product due to the complete exhaustion of the
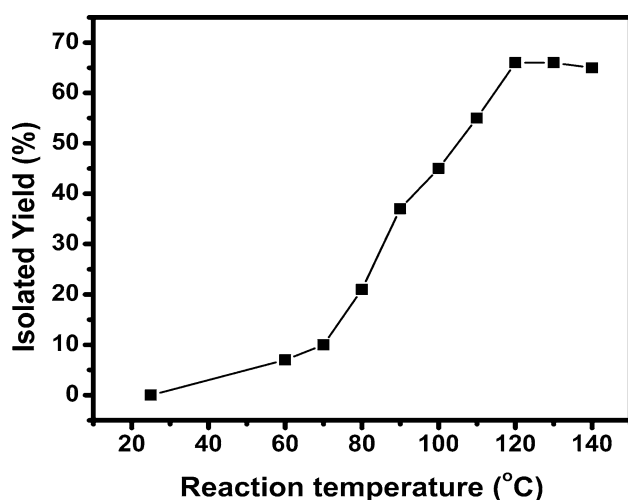
Fig. 7 Influence of reaction time on the isolated yield for styrene in reaction product (Reaction conditions; Catalyst amount 20 mg, Temp. 120 °C with TFA)

oxidizing agent in the reaction mixture [39]. Taking energy consideration, the 24 h reaction time is found appropriate for this reaction model with better efficiency for benzaldehyde production.

3.2.4 Influence of solvents

Table 4 shows the effect of the solvent (methanol to water ratio) on the selectivity of the benzaldehyde in the model reaction. As we know that the water is not an organic solvent, and it shows less or nearly zero solubility with the majority of organics. The optimization is done with the optimum amount of catalyst (20 mg) along with TFA as an oxidizing agent at 120 °C for 24 h reaction time.

Water (MW 18.015, density 1.00 g/ml, melting point 0 °C, boiling point 100 °C.) is considered as a "polar protic solvent," which contains one or more hydrogen atoms that can be vanished as a proton in a transfer reaction. Mostly water is used with many polar organic co-solvents (methanol, ethanol, acetone, etc.) to enhance the solubility along with the properties of water itself [43]. Initially, it depicts negligible selectivity for benzaldehyde. It may be due to the insolubility of styrene with water. Due to the environmental advantages of water compared with hazardous organic solvents, the water along with methanol (MW 32.042, density 0.791 g/ml, melting point − 98 °C, and boiling point 65 °C) is selected as a co-solvent. The solvent (water) having high dielectric constant helps styrene conversion, and the solvent (methanol) having low dielectric constant helps the formation of benzaldehyde. Further, the addition of methanol results in increasing the selectivity and yield up to 66%

Fig. 6 Influence of reaction temperature on the isolated yield for styrene in reaction product (Reaction conditions; Catalyst amount 20 mg, Time 24hrs with TFA)

for benzaldehyde at 3:2 (MeOH: Water). Among various ratio of methanol and water, it is found that the optimized value of selectivity for benzaldehyde is obtained at MeOH:Water—3:2 ratio.

3.2.5 Influence of oxidizing agent

Table 5 shows the effect of various acids as an oxidizing agent for the selectivity of the benzaldehyde in the oxidation of styrene with optimized reaction conditions. The selectivity of benzaldehyde with different oxidizing acids like p-toluene sulfonic acid (PTSA) [44], terephthalic acid [44], phosphoric acid [43], pivalic acid [45], tri-fluoro acetic acid [46], nitric acid [47], and acetic acid [48] are analyzed. The best selectivity of benzaldehyde is found with TFA in optimized reaction conditions.

3.2.6 Influence of cerium content on catalytic activity

Table 6 displays the performance of the individual catalyst for benzaldehyde production through styrene oxidation within similar optimized conditions. As it is revealed that all these ferrite samples can proficiently catalyze the oxidation of styrene and benzaldehyde is confirmed as the foremost product in all cases. The results reveal that the Ce-doped barium hexaferrite powders show higher performance as compared to undoped $Ba_2Co_2Fe_{12}O_{22}$ ferrite. The $Ba_{1.8}Ce_{0.2}Co_2Fe_{12}O_{22}$ composition shows the best performance within the model reaction with the highest yield (71%) for the desired product (benzaldehyde). Further increasing in cerium content doesn't provide good selectivity due to the larger crystallite size (confirmed using XRD), resulting in lower surface area as compared to the $x = 0.2$ sample. Hence in the case of $x = 0.3$, less number of active sites (surface oxygen vacancies) available to provide oxidation of styrene and results in lower benzaldehyde selectivity.

Table 4 Influence of solvent on styrene oxidation

S. no.	Solvent ratio (MeOH:Water)	Catalyst	Cat. Amt (mg)	Oxidizing agent	Temp (°C)	Time (h)	Yield (%)
1	0:1	Barium hexaferrite	20	TFA	120	24	Trace
2	1:0	Barium hexaferrite	20	TFA	120	24	32
3	1:1	Barium hexaferrite	20	TFA	120	24	16
4	2:1	Barium hexaferrite	20	TFA	120	24	46
5	3:2	Barium hexaferrite	20	TFA	120	24	66
6	1:2	Barium hexaferrite	20	TFA	120	24	Trace
7	2:3	Barium hexaferrite	20	TFA	120	24	12

Table 5 Influence of oxidizing agent on styrene oxidation

S. no.	Catalyst	Cat. Amt (mg)	Oxidizing agent	Temp (°C)	Time (h)	Yield (%)
1	Barium hexaferrite	20	PTSA	120	24	40
2	Barium hexaferrite	20	Pivalic acid	120	24	00
3	Barium hexaferrite	20	Terephthalic acid	120	24	Trace
4	Barium hexaferrite	20	TFA	120	24	66
5	Barium hexaferrite	20	HNO_3	120	24	00
6	Barium hexaferrite	20	H_3PO_4	120	24	Trace
7	Barium hexaferrite	20	H_2SO_4	120	24	00
8	Barium hexaferrite	20	Acetic acid	120	24	35

Table 6 Performance of as-prepared samples over the oxidation of styrene at optimized conditions

S. no.	Catalyst	Cat. Amt (mg)	Oxidizing agent	Temp (°C)	Time (h)	Yield (%)
1	$Ba_2Co_2Fe_{12}O_{22}$	20	TFA	120	24	66
2	$Ba_{1.9}Ce_{0.1}Co_2Fe_{12}O_{22}$	20	TFA	120	24	68
3	$Ba_{1.8}Ce_{0.2}Co_2Fe_{12}O_{22}$	20	TFA	120	24	71
4	$Ba_{1.7}Ce_{0.3}Co_2Fe_{12}O_{22}$	20	TFA	120	24	69

3.2.7 X-ray photoelectron spectroscopy

XPS technique (from 1350 to 1 eV) is employed to examine the chemical composition of the surface elements in the as-prepared cerium-doped barium hexaferrite ($Ba_{1.8}Ce_{0.2}Co_2Fe_{12}O_{22}$) sample, found best to achieve the highest selectivity for benzaldehyde. As demonstrated in wide scan XPS spectra (Fig. 8a), the sample contains Ba, Ce, Fe, Co, and O elements, and no other contamination element is identified in the spectrum except carbon. The C1s peak is attuned to 284.8 eV and is considered as an internal standard for rectifying the binding energy for the other peaks [49]. Figure 8b shows the high-resolution signal of Ba^{2+} 3d XPS spectra and confirms the presence of Ba^{2+} oxidation state by two broad peaks with corresponding binding energies of $Ba_{3d5/2}$ (779.5 eV) and $Ba_{3d3/2}$ (794.9 eV), respectively [50]. Figure 8c illustrate a characteristic 3d spectrum of Ce^{3+} and Ce^{4+} ionic blend. Characteristic peaks of the Ce^{4+}_{3d} and Ce^{3+}_{3d} ion can be observed at 899.4 eV and 901.8 eV, respectively. Additionally, the peaks for $Ce^{4+}_{3d5/2}$ (884.9 eV), $Ce^{3+}_{3d5/2}$ (888.1 eV), $Ce^{3+}_{3d3/2}$ (907.6 eV) and $Ce^{4+}_{3d3/2}$ (918.0 eV) have also been recognized within the sample [51, 52]. The analysis for the Co 2p spectrum in the sample becomes much more complicated due to the coexistence of intensive Ba 3d spectrum within the same range of binding energies (780 to 795 eV). Figure 8d) clarifies the presence of Co^{2+} with two symmetric peaks corresponding to peak position for $Co^{2+}_{2p3/2}$ (779.7 eV) and $Co^{2+}_{2p1/2}$ (795.0 eV) spectrum associated with two satellite peaks at 782.2 and 803.8, respectively [53, 54]. The incorporation of cerium in the sample leads to the coexistence of Fe^{2+} and Fe^{3+} oxidation states, which are confirmed by the Fe 2p spectra. As shown in Fig. 8e, two broad peaks associated with $Fe_{2p3/2}$ and $Fe_{2p1/2}$ peaks can be detected at 710.5 eV and 723.9 eV along with two satellite peaks at 719.0 and 733.0 eV, respectively. These broad peaks for $Fe_{2p3/2}$ and $Fe_{2p1/2}$ are found to be a combination of two peaks in each at $Fe^{2+}_{2p3/2}$(710.3 eV), $Fe^{3+}_{2p3/2}$ (712.0 eV), and $Fe^{2+}_{2p1/2}$(723.5 eV), $Fe^{3+}_{2p1/2}$(724.94 eV), respectively [55, 56]. The high-resolution XPS spectrum for O1s confirms the presence of O_2-oxidation state (Fig. 8f) at the binding energy of 529.8 eV, native oxygen vacancy by the peak at 531.7 eV and surface oxygen (due to the presence of H_2O or $–CO_3$ bonds on the surface) by the peak at 533.3 eV [38, 46, 47]. The peak associated with oxygen vacancy is agreed with the XRD results for $Ba_{1.8}Ce_{0.2}Co_2Fe_{12}O_{22}$, which shows that the addition of Ce ions results in the lattice contraction and generates the oxygen vacancies. It can be concluded that the coexistence of Fe^{2+}, Fe^{3+}, and Ce^{3+}, Ce^{4+} ions in the sample causes the formation of oxygen vacancies with the substitution of Ce ions. The availability of surface oxygen vacancies is observed as the supreme reactive sites in catalysis. These oxygen vacancies are found to stimulate the disintegration of water molecules into active OH radicals, providing the opportunity

to develop a vigorous catalyst in the presence of water vapor [57–60]. The higher selectivity for benzaldehyde can be explained due to the presence of an oxygen vacancy cluster, which leads to a faster oxidation rate and doesn't allow further dissociation of the desired product. This increasing trend for benzaldehyde selectivity for $Ba_{1.8}Ce_{0.2}Co_2Fe_{12}O_{22}$ can also be linked to the presence of a well-known oxidation catalyst CeO_2 in the samples (as an impurity phase, confirmed by XRD). It provides easy coordination of organic ligands on Ce^{3+} active sites of CeO_2 [12]. The lower value of selectivity and conversion in the case of $Ba_{1.7}Ce_{0.3}Co_2Fe_{12}O_{22}$ may be due to fewer oxygen vacancies in the active sites of the catalyst. Due to the highest benzaldehyde selectivity among all the prepared ferrite samples, the sample $Ba_{1.8}Ce_{0.2}Co_2Fe_{12}O_{22}$ is preferred as a catalyst to analyze further for its reproducibility and substrate scope.

3.2.8 Reprocess of the ferrite (catalyst)

After the optimization of reaction conditions in model reaction, the catalyst $Ba_{1.8}Ce_{0.2}Co_2Fe_{12}O_{22}$ can be easily separated by the application of a magnetic field at the tube surface from the reaction mass. After separation, the same powder is used for the second run with the same optimized conditions. The selectivity of the benzaldehyde doesn't affect remarkably; a slight decrement is noticed, as shown in Fig. 9. It may be due to the inevitable losses associated with the separation process of catalyst. The optimization is done with the optimum amount of catalyst (20 mg) along with TFA as an oxidizing agent and solvent (MeOH:Water—3:2) at 120 °C for 24 h reaction time. So, the Ce-doped barium hexaferrite can be considered as a promising material in the selective oxidation of styrene, along with its better recyclability and benzaldehyde selectivity approx-71%.

3.2.9 Substrates scope at optimized conditions

Table 7 displays the results of the selective oxidation of various substrates using $Ba_{1.8}Ce_{0.2}Co_2Fe_{12}O_{22}$ ferrite sample underneath with optimized conditions for the model reaction. It can successfully catalyze the oxidation of other cyclic olefins likewise 4-methylstyrene, 4-chlorostyrene, 2,4-dimethyl-styrene, 2-vinylnaphthalene, 4-methoxystyrene. Generally, it shows good selectivity of concerning products (more than 50% in all cases) and particularly shows 69% selectivity for 4-methylbenzaldehyde and 70% for 2-Naphthaldehyde.

4 Conclusion

Cerium-doped nanocrystalline Y-type barium hexaferrite is successfully synthesized using sol–gel auto combustion with metal-nitrates as precursors. This ferrite system can be
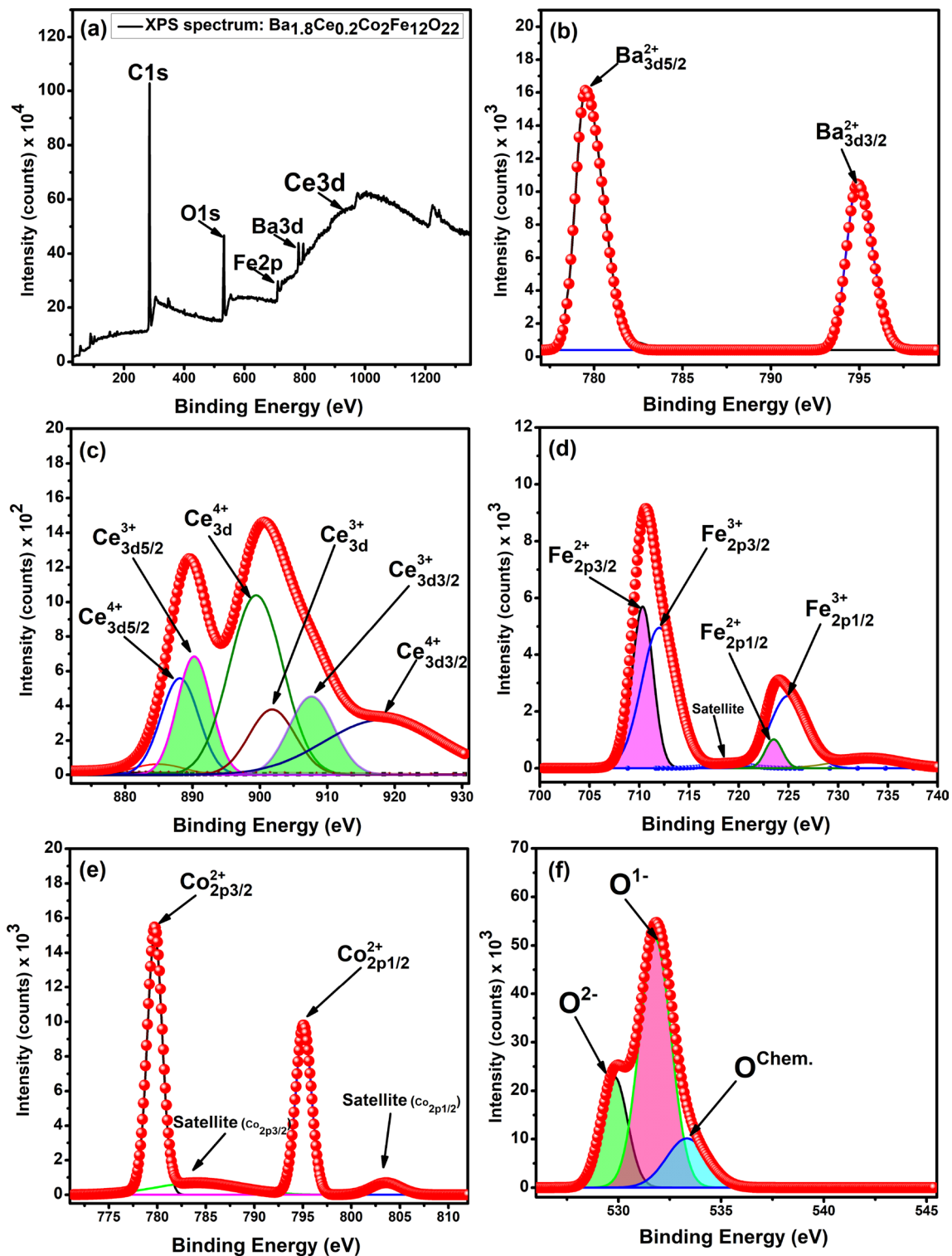
Fig. 8 The XPS spectra of $Ba_{1.8}Ce_{0.2}Co_2Fe_{12}O_{22}$ surface **a** wide scan photoelectron spectra with high resolution spectrum corresponding to **b** Ba-3d, **c** Ce-3d, **d** Fe-2p, **e** Co-2p, **f** O-1s regions
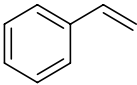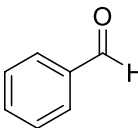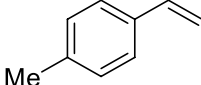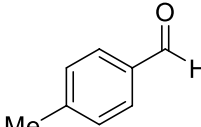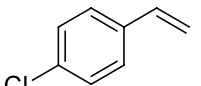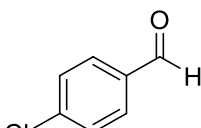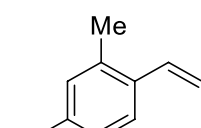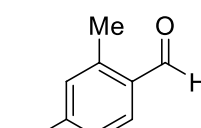
selected as industrially adoptable catalysts for styrene oxidation reaction, and the production of benzaldehyde. This work indicates that the catalytic activity of the complex ferrite is

not only limited up to conventionally use soft ferrites but also it can be applied to some sort of hard ferrites. The as-prepared cerium-doped barium hexaferrite shows excellent
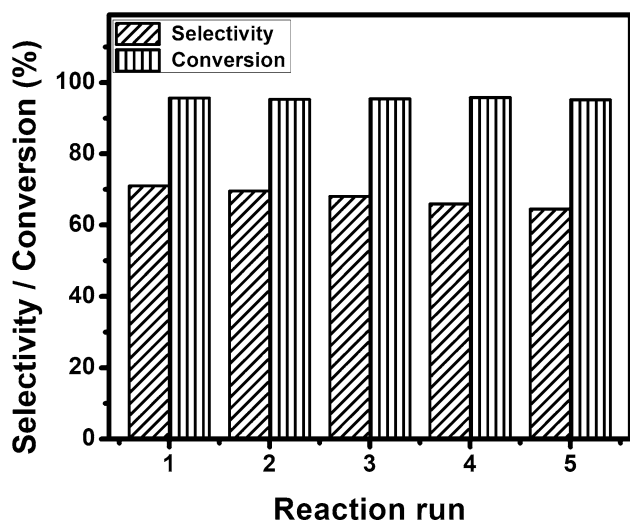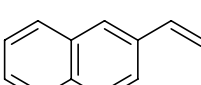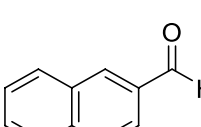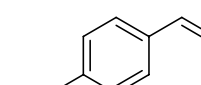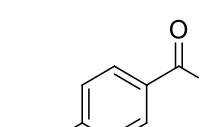
Fig. 9 Reprocess of the catalyst $Ba_{1.8}Ce_{0.2}Co_2Fe_{12}O_{22}$ ferrite

Table 7 Substrates scope at optimized conditions for $Ba_{1.8}Ce_{0.2}Co_2Fe_{12}O_{22}$ ferrite

S. No	Reactant	Product	Benzaldehyde yield (%)
1			71
2			58
3			69
4			55
5			70
6			50

catalytic performance because of their high surface area and large dispersity, which provides additional active sites for the reaction with trifluoroacetic acid (TFA) as an oxidant. A raise in styrene conversion is found with an increment in temperature. The optimum result shows that 20 mg of $Ba_{1.8}Ce_{0.2}Co_2Fe_{12}O_{22}$ ferrite displays a 71% yield for benzaldehyde at 120 °C for 24 h. The higher selectivity for benzaldehyde can be explained due to the presence of an oxygen vacancy cluster. The catalyst is magnetically separable to reprocess. There is no remarkable loss of catalytic activity when it is reprocessed for five consecutive trials. It is concluded that the cerium-doped Y-type barium hexaferrite can also be used as a promising material in diverse oxidation reactions.

References

1. R.B. Jotania, H.S. Virk, Structural, dielectric and magnetic properties, solid state phenomena. Solid State Phenom. **189**, 209–232 (2012)
2. J. Tasca, A. Lavat, K. Nesprias, G. Barreto, E. Alvarez, N. Eyler, A. Cañizo, Cyclic organic peroxides thermal decomposition in the presence of $CuFe_2O_4$ magnetic nanoparticles. J. Mol. Catal. A **363–364**, 166–170 (2012)
3. C. Black, R.R. Spence, K. Whiston, S. Sproules, S.D. Jackson, Effect of excess iron on oxidative dehydrogenation of 1-butene over a series of zinc ferrite catalysts. Progr. Petrochem. Sci. **2**(2), 168–189 (2018)
4. Y.M. Chung, Y.T. Kwon, T.J. Kim, S.J. Lee, S.H. Oh, Prevention of catalyst deactivation in the oxidative dehydrogenation of n-butene to 1,3-butadiene over Zn-ferrite catalysts. Catal. Lett. **131**(3–4), 579–586 (2009)
5. D. Fino, N. Russo, G. Saracco, V. Specchia, CNG engines exhaust gas treatment via Pd-Spinel-type-oxide catalysts. Catal. Today **117**, 559–563 (2006)
6. E. Casbeer, V.K. Sharma, X.-Z. Li, Synthesis and photocatalytic activity of ferrites under visible light: a review. Sep. Purif. Technol. **87**, 1–14 (2012)
7. F. Papa, L. Patron, O. Carp, C. Paraschiv, Catalytic activity of neodymium substituted zinc ferrites for oxidative conversion of methane. J. Mol. Catal. A **299**, 93–97 (2009)
8. D. Guin, B. Baruwati, S.V. Manorama, A simple chemical synthesis of nanocrystalline AFe_2O_4 (A = Fe, Ni, Zn): an efficient catalyst for selective oxidation of styrene. J. Mol. Cata. A **242**, 26–31 (2005)
9. Q. Yang, C. Li, S. Yuan, J. Li, P. Ying, Q. Xin, W. Shi, Epoxidation of styrene on a novel titanium-silica catalyst prepared by ion beam implantation. J. Catal. **183**, 128–130 (1999)
10. J.M. Mitchell, N.S. Finney, New molybdenum catalysts for alkyl olefin epoxidation their implications for the mechanism of oxygen atom transfer. J. Am. Chem. Soc. **123**, 862–869 (2001)
11. N.T. Thao, N.D. Trung, D.V. Long, Activity of molybdate-intercalated layered double hydroxides in the oxidation of styrene with air. Catal. Lett. **146**, 918–928 (2016)

12. J. Tong, W. Li, L. Bo, H. Wang, Y. Hu, Z. Zhang, Abdulla Mahboob, Selective oxidation of styrene catalyzed by cerium-doped cobalt ferrite nanocrystals with greatly enhanced catalytic performance. J. Catal. **344**, 474–481 (2016)

13. S.K. Pardeshi, R.Y. Pawar, $SrFe_2O_4$ complex oxide an effective and environmentally benign catalyst for selective oxidation of styrene. J. Mol. Catal. A **334**, 35–43 (2011)

14. N. Ma, Y. Yue, W. Hua, Z. Gao, Selective oxidation of styrene over nanosized spinel-type $Mg_xFe_{3-x}O_4$ complex oxide catalysts. Appl. Catal. A **251**, 39–47 (2003)

15. S.K. Pardeshi, R.Y. Pawar, Optimization of reaction conditions in selective oxidation of styrene over fine crystallite spinel-type $CaFe_2O_4$ complex oxide catalyst. Mater. Res. Bull. **45**(5), 609–615 (2010)

16. R. Ramanathan, S. Sugunan, Styrene oxidation by H_2O_2 using Ni–Gd ferrites prepared by co-precipitation method. Catal. Commun. **8**(10), 1521–1526 (2007)

17. X. Cai, H. Wang, Q. Zhang, J. Tong, Selective oxidation of styrene efficiently catalyzed by spinel Mg–Cu ferrite complex oxides in water. J. Sol-Gel Sci. Technol. **69**, 33–39 (2014)

18. G. Evans, I.V. Kozhevnikov, E.F. Kozhevnikova, J.B. Claridge, R. Vaidhyanathan, C. Dickinson, C.D. Wood, A.I. Cooper, M.J. Rosseinsky, Particle size–activity relationship for $CoFe_2O_4$ nanoparticle CO oxidation catalysts. J. Mater. Chem. **18**, 5518–5523 (2008)

19. F. Shi, M.K. Tsea, M.-M. Pohl, J. Radnikc, A. Brückner, S. Zhang, M. Beller, Nano-iron oxide-catalyzed selective oxidations of alcohols and olefins with hydrogen peroxide. J. Mol. Catal. A **292**, 28–35 (2008)

20. N.M.R. Martins, A.J.L. Pombeiro, L.M.D.R.S. Martin, A green methodology for the selective catalytic oxidation of styrene by magnetic metal-transition ferrite nanoparticles. Catal. Commun. **116**, 10–15 (2018)

21. A. Dhakshinamoorthy, M. Alvaro, H. Garcia, Aerobic oxidation of styrenes catalyzed by an iron metal organic framework. ACS Catal. **1**(8), 836–840 (2011)

22. M. Nemanashi, R. Meijboom, Dendrimer derived, titania-supported Au nanoparticles as potential catalysts in styrene oxidation. Catal. Lett. **143**, 324–332 (2013)

23. A.B. Justinus, L.K. Satrio, Production of benzaldehyde: a case study in a possible industrial application of phase-transfer catalysis. Chem. Eng. J. **82**, 43–56 (2001)

24. N.M. McNeil, C. McDonnell, M. Hambrook, T.G. Back, Oxidation of disulfides to thiolsulfinates with hydrogen peroxide and a cyclic seleninate ester catalyst. Molecules **20**, 10748–10762 (2015)

25. National Center for Biotechnology Information. PubChem Database. Trifluoroacetic acid, CID=6422, https://pubchem.ncbi.nlm.nih.gov/compound/Trifluoroacetic-acid Accessed May 30, 2019.

26. N. Adeelaa, U. Khanb, M. Iqbal, S. Riaz, M. Irfan, H. Ali, K. Javed, I. Bukhtiar, K. Maaz, S. Naseem, Structural and magnetic response of Mn substituted Co_2Y type barium hexaferrites. J. Alloy Compd. **686**, 1017–1024 (2016)

27. İ. Araz, Electromagnetic properties of Ce substituted barium hexaferrite in X band frequencies. J. Mater. Sci. **30**, 14935 (2019)

28. Z. Mosleh, P. Kameli, A. Poorbaferani, M. Ranjbar, H. Salamati, Structural, magnetic and microwave absorption properties of Ce-doped barium hexaferrite. J. Magn. Magn. Mater. **397**, 101 (2016)

29. Z. Vakil, Effect of Cerium (Ce^{3+}) doping on structural, magnetic and dielectric properties of Barium Ferrite ($BaFe_{12}O_{19}$), IEEE International Conference on Electrical, Computer and Communication Technologies (ICECCT) (2015).

30. V. Chaudhari, S.E. Shirsath, M.L. Mane, R.H. Kadam, S.B. Shelke, D.R. Mane, Crystallographic, magnetic and electrical properties of $Ni_{0.5}Cu_{0.25}Zn_{0.25}La_xFe_{2-x}O_4$ nanoparticles fabricated by sol–gel method. J. Alloys Compd. **549**, 213–220 (2013)

31. M.A. Almessierea, Y. Slimanib, M. Sertkold, M. Nawazc, A. Baykalc, I. Ercanb, The impact of Zr substituted Sr hexaferrite: investigation on structure, optic and magnetic properties. Results Phys. **13**, 102244 (2019)

32. J. Temuujin, M. Aoyama, M. Senna, T. Masuko, C. Ando, H. Kishi, Synthesis of Y-type hexaferrites via a soft mechanochemical route. J. Solid State Chem. **177**, 3903–3908 (2004)

33. D. Shekhawat, P.K. Roy, Impact of yttrium on the physical, electro-magnetic and dielectric properties of auto-combustion synthesized nanocrystalline strontium hexaferrite. J. Mater. Sci. **30**, 1187–1198 (2019)

34. Z. Lalegani, A. Nemati, Effects of Ce–Co substitution on structural, magnetic and dielectric properties of M-type barium hexaferrite nanoparticles synthetized by sol–gel auto-combustion route. J. Mater. Sci. **26**, 2134–2144 (2015)

35. M. Abbas, B.P. Rao, M.N. Islam, K.W. Kim, S.M. Naga, M. Takahashi, C. Kim, Size-controlled high magnetization $CoFe_2O_4$ nanospheres and nanocubes using rapid one-pot sonochemical technique. Ceram. Int. **40**(2), 3269–3276 (2014)

36. C.-J. Li, B. Wang, J.-N. Wang, Magnetic and microwave absorbing properties of electrospun $Ba_{(1-x)}La_xFe_{12}O_{19}$ nanofibers. J. Magn. Magn. Mater. **324**, 1305–1311 (2012)

37. S. Singh, N. Sangwa, Structural and magnetic properties of nickel ferrite nanoparticles synthesized by ball milling. Int. J. Eng. Sci. Invent. **6**(10), 36–39 (2017)

38. J.R.L. Smith, Y. Iamamoto, F.S. Vinhado, Oxidation of alkanes by iodosylbenzene (PhIO) catalysed by supported Mn(III) porphyrins: activity and mechanism. J. Mol. Catal. A **252**, 23–30 (2006)

39. R.Y. Pawar, S.K. Pardeshi, Selective oxidation of styrene to benzaldehyde using soft $BaFe_2O_4$ synthesized by citrate gel combustion method. Arab J. Chem. **11**(2), 282–290 (2014)

40. M.V. Vishnetskaya, IYu Yakimova, I.A. Sidorenkova, The catalytic oxidation of organic compounds in superacids. Russ. J. Phys. Chem. **80**(2), 176–180 (2006)

41. M. AliNasseri, A. Allahresani, H. Raissi, Mild oxidation of alkenes catalyzed by Fe_3O_4/SiO_2 nanoparticles. React. Kinetics Mech. Catal. **112**, 397–408 (2014)

42. M. Kooti, M. Afshari, Magnetic cobalt ferrite nanoparticles as an efficient catalyst for oxidation of alkenes. Sci Iran. **19**(6), 1991–1995 (2012)

43. Dr. P.G. Hultin, A Guide to Solvents and Reagents in Introductory Organic Chemistry for students in 2.222, https://home.cc.umanitoba.ca/~hultin/chem2220/Support/solvents_and_reagents.pdf.

44. N. Li, Y. Gao, X. Zhang, Z. Yu, L. Shi, Q. Sun, Oxidation of styrene to benzaldehyde by p-toluenesulfonic acid using hydrogen peroxide in the presence of activated carbon. Chin. J. Catal. **36**, 721–727 (2015)

45. H. Toledo, E. Pisarevsky, A. Abramovich, A.M. Szpilman, Organocatalytic oxidation of aldehydes to mixed anhydrides. Chem. Commun. **49**, 4367–4369 (2012)

46. R.A. Kjonaas, A.E. Clemons, The Baeyer–Villiger oxidation with trifluoroacetic acid and household sodium percarbonate. J. Chem. Educ. **85**, 827–828 (2008)

47. A. Onopchenko, J. G. D. Schulz, Process for Converting Styrene or Polystyrene to Nitrobenzoic Acids, United States Patent-3978118A (1976).

48. M. Hirano, E. Kitamura, T. Morimoto, Oxidation by cobalt(III) acetate. Part 2.l Oxidation of styrene in acetic acid. J. Chem. Soc. Perkin Trans. **2**, 569–573 (1980)

49. L.Q. Wu, Y.C. Li, S.Q. Li, Z.Z. Li, G.D. Tang, W.H. Qi, L.C. Xue, X.S. Ge, L.L. Ding, Method for estimating ionicities of oxides using O1s photoelectron spectra. AIP Adv. **5**, 097210 (2015)

50. G.A. Ashraf, R.T. Rasool, Md Hassan, L. Zhang, Enhanced photo Fenton-like activity by effective and stable AleSmMhexaferrite-heterogenous catalyst magnetically detachable for methylene blue degradation. J. Alloy. Compd. **821**, 153410 (2020)

51. S.I. Ahmad, D.R. Kumar, I.A. Syed, R. Satar, S.A. Ansari, Structural, spectroscopic and magnetic study of nanocrystalline cerium-substituted magnesium ferrites. Arab. J. Sci. Eng. **42**, 389–398 (2017)

52. F. Chen, X. Wang, Y. Nie, Q. Li, J. Ouyang, Z. Feng, Y. Chen, V.G. Harris, Ferromagnetic resonance induced large microwave magnetodielectric effect in cerium doped $Y_3Fe_5O_{12}$ ferrites. Sci. Rep. **6**, 28206 (2016)

53. M. Fantauzzi, F. Secci, M.S. Angotzi, C. Passiu, C. Cannas, A. Rossi, Nanostructured spinel cobalt ferrites: Fe and Co chemical state, cation distribution and size effects by X-ray photoelectron spectroscopy. RSC Adv. **9**, 19171 (2019)

54. J. Zemek, P. Papakonstantinou, R. Atkinson, Magneto-optical and XPS spectra of cobalt and titanium substituted hexaferrite films. J. Magn. Soc. Jpn. **20**, 117–120 (1996)

55. Z. Zhou, Y. Zhang, Z. Wang, W. Wei, W. Tang, J. Shi, R. Xiong, Electronic structure studies of the spinel $CoFe_2O_4$ by X-ray photoelectron spectroscopy. Appl. Surf. Sci. **254**, 6972–6975 (2008)

56. S. Liu, Z. Dong, D. Xiang, Y. Jiang, Q. Tao, Y. Cao, Crossing-link of experimental reducibility tests, XPS characterizations and DFT estimates on ferrite oxygen carriers in CLC. Appl. Catal. B **238**, 647–655 (2018)

57. A. Younis, S.E. Shirsath, B. Shabbir, S. Li, Controllable dynamics of oxygen vacanciesthrough extrinsic doping for superior catalytic activities. Nanoscale **10**, 18576 (2018)

58. J.H. Kim, Y.J. Jang, J.H. Kim, J.-W. Jang, S.H. Choi, J.S. Lee, Defective $ZnFe_2O_4$ nanorods with oxygen vacancy for photoelectrochemical water splitting. Nanoscale **7**, 19144 (2015)

59. S.B.T. Tran, H. Choi, Oh Sunyoung, Jeong Young Park, Defective Nb_2O_5-supported Pt catalysts for CO oxidation: Promoting catalytic activity via oxygen vacancy engineering. J. Catal. **375**, 124–134 (2019)

60. L. Li, X. Feng, Y. Nie, S. Chen, F. Shi, K. Xiong, W. Ding, X. Qi, J. Hu, Z. Wei, L.J. Wan, Insight into the effect of oxygen vacancy concentration on the catalytic performance of MnO_2. ACS Catal. **5**, 4825–4832 (2015)

Publisher's Note Springer Nature remains neutral with regard to jurisdictional claims in published maps and institutional affiliations.